Revision 2

Using cathodoluminescence to identify oscillatory zoning of perthitic K-feldspar from the equigranular Toki granite

Takashi Yuguchi[a,*], Mai Nonaka[a], Satoshi Suzuki[a], Takumi Imura[a], Kazuo Nakashima[a], Tadao Nishiyama[b]

[a]Faculty of Science, Yamagata University, 1-4-12 Kojirakawa, Yamagata 990-8560, Japan

[b]Faculty of Advanced Science and Technology, Kumamoto University, 2-39-1, Kurokami, Chuo-ku, Kumamoto 860-8555, Japan

*Corresponding author: T. Yuguchi

E-mail address: takashi_yuguchi@sci.kj.yamagata-u.ac.jp

Tel: +81 23 628 4641/Fax: +81 23 628 4661

Abstract

For the first time, cathodoluminescence (CL) was used to show oscillatory zoning in perthitic K-feldspars from the equigranular Toki granite, central Japan. Based on the CL patterns, two types of zoning are identified: single core oscillatory zoning (SCOZ) and multiple core oscillatory zoning (MCOZ). The SCOZ is defined by oscillatory zoning around a single crystal core within the K-feldspar crystal, whereas the MCOZ depicts two or more such crystal cores. The crystal cores displayed in CL images reflect the nucleation parts of magmatic K-feldspar. The existence of MCOZ patterns in K-feldspars indicates multiple nucleii. CL patterns reveal crystal growth behavior of magmatic K-feldspar in the equigranular Toki granite. CL intensities are positively correlated with titanium and barium concentrations, indicating that the CL variations depend on two factors: 1) titanium concentration as a CL activator and 2) density of Al-O^{-}-Al structural defects. The analysis of CL images revealed that albite-rich phases in microperthite and patchperthite with low luminescence intensities cut across the CL bands of the oscillatory zoning, indicating that the oscillatory zoning in the orthoclase-rich host phase of K-feldspar was not perturbed by the formation of microperthite and patchperthite in the post-crystallization stage. The luminescence intensities of albite-rich phases in patchperthite are lower than those in microperthite, which is due to the differences in titanium and barium concentrations between them. In the post-crystallization stage, the mass transfer of titanium and barium occurred during the formation of microperthite and patchperthite. Therefore, the difference in the luminescence intensities between microperthite and patchperthite lamellae reflects their different formation mechanisms between exsolution coarsening and dissolution–

precipitation coarsening. In summary, CL analyses can be used for the evaluation of the nucleation and growth not only of anhedral K-feldspar crystals in equigranular granite but also of K-feldspar phenocrysts/megacrysts in porphyritic granite. It can reveal the spatial extent of element partitioning between the melt and crystal, along with that of mass transfer from the melt into crystals during the magma evolution. Moreover, the CL analyses can also be used for the interpretation of K-feldspar textural development during the post-crystallization stage.

Keywords: cathodoluminescence, K-feldspar, oscillatory zoning, microperthite, patchperthite, granite.

Introduction

Oscillatory zoning is defined as multiple growth layers that are generally parallel to crystallographic planes and range in thickness from tens of nanometers to several tens of micrometers (Shore and Fowler, 1996). Potassium feldspar (K-feldspar) is one of the most common minerals in felsic plutonic rocks. Oscillatory zoning is frequently observed in K-feldspar megacrysts and phenocrysts under polarized light (Vernon and Paterson, 2008; Vernon, 2010) as well as in backscattered electron images (BSE; Landi et al., 2019). For example, in granitic rocks from the Sierra Nevada batholith, K-feldspar megacrysts of igneous origin show elemental oscillatory zoning marked by varying concentrations of BaO, which range from 0.5 wt% to 3.5 wt% (Moore and Sisson, 2008). K-feldspar phenocrysts in porphyritic Half Dome and Cathedral Peak granodiorite from the Tuolumne intrusion also show elemental oscillatory zoning with BaO concentrations ranging from <0.5 wt% to ~2 wt% (Johnson and Glazner, 2010; Glazner and Johnson, 2013).

Cathodoluminescence (CL) patterns of minerals in granite can be used to reveal mineral genesis and growth, which also contribute to clarifying the intrusion, emplacement, and cooling processes of granitic magma (Marshall, 1988; Nakano et al., 2005; Kayama et al., 2010) and the magma evolution (Yuguchi et al., 2020). In previous CL studies of K-feldspar in granite, Kayama et al. (2010) characterized the CL emission centers in K-feldspar from the Cerro Balmaceda pluton syenite and observed CL heterogeneity in K-feldspar. Lee et al. (2007) and Parsons et al. (2008) reported that albite-rich patches in perthitic K-feldspar from the Klokken syenite display oscillatory zoning in CL images. Perthitic K-feldspar consists of albite-rich phases (patch and lamella) in orthoclase-rich host phases. Oscillatory

DOI: https://doi.org/10.2138/am-2022-8146. http://www.minsocam.org/

zoning in orthoclase-rich host phases of K-feldspar megacrysts and phenocrysts was reported by several previous CL studies (e.g., Słaby et al., 2008; Higgins, 2017; Oppenheim et al., 2021). K-feldspar phenocrysts from porphyritic Half Dome and Cathedral Peak granodiorites display CL oscillatory zoning in the orthoclase-rich host phase under optical-CL observations (cold-cathode color cathodoluminescence stage attached to stereoscope) (Oppenheim et al., 2021). Higgins (2017) presented cathodoluminescence images of K-feldspar megacrysts from the Cathedral Peak granodiorite based on optical-CL observation (cold-cathode color cathodoluminescence instrument mounted on a petrographic microscope), displaying CL oscillatory zoning in the orthoclase-rich host phase. CL oscillatory zoning of K-feldspar phenocrysts (without perthitic texture) in microgranular magmatic enclaves in the Karkonosze granite was found based on optical-CL observations (hot-cathode instrument attached to digital microscope) (Słaby et al., 2008). Słaby et al. (2008) revealed a positive correlation between CL intensity and barium concentrations, indicating that the differences in CL intensities are attributed to Al-O^{-}-Al structural defects due to coupled KSi–BaAl exchange.

However, to the best of our knowledge, CL oscillatory zoning of an orthoclase-rich host phase has never been reported in anhedral K-feldspar from equigranular granitic rocks. Large K-feldspar megacrysts in granites grow at super-solidus conditions in a low-temperature magma chamber (e.g., Moore and Sisson, 2008) or even at sub-solidus conditions (e.g., Vernon and Paterson, 2008), and large K-feldspar phenocrysts crystallize in a high-temperature magma chamber (Vernon, 1986). For the formations of megacrysts and phenocrysts, wide space between previously crystallized minerals is required.

Conversely, the anhedral magmatic K-feldspar in equigranular granite studied here grew in limited space between previously crystallized minerals. Thus, the environment (and stage) at which anhedral K-feldspar grows in equigranular granite differs from that of K-feldspar megacrysts and phenocryst formation. In this work, we used CL imaging to observe oscillatory zoning of the orthoclase-rich host phase in anhedral perthitic K-feldspar from the equigranular Toki granite, central Japan. This study reports on: 1) characterization of the CL patterns of anhedral magmatic K-feldspar from the Toki granite to gain insights on its nucleation and growth, and 2) characterization of the CL patterns of post-crystallization textures such as veins, microperthite, and patchperthite, which enhances our understanding of the textural development during the post-crystallization stage.

The Toki granite

The Toki granite in the Tono district of central Japan is one of the Late Cretaceous plutonic bodies of the Inner Zone of the Southwest Japan Arc (Fig. 1A; Ishihara and Chappell, 2007). The Toki granite is a ~14 × 12 km^2 stock (Ishihara and Suzuki, 1969) that intruded into the Jurassic sedimentary rocks of the Kamiaso Formation in the Mino Terrane (Sano et al., 1992) and into the Late Cretaceous Nohi rhyolite (Sonehara and Harayama, 2007; Fig. 1B). The equigranular Toki granite is a concentrically zoned pluton, which is characterized by three rock facies grading from muscovite–biotite granite (MBG) at the margin through hornblende–biotite granite (HBG) in the interior to biotite granite (BG) in the core (Fig. 1C). Studies by Shibata and Ishihara (1979) and Suzuki and Adachi (1998) revealed that the Toki granite has a whole-rock Rb-Sr isochron age of 72.3 ± 3.9 Ma and a monazite chemical Th-U-total Pb isochron (CHIME) age of 68.3 ± 1.8 Ma. Thermochronological data have been reported for samples collected at multiple sampling sites within the Toki granite: zircon U–Pb ages ranging from 74.7 ± 4.2 to 70.4 ± 1.7 Ma (N = 14: Yuguchi et al., 2016; 2019), biotite K–Ar ages from 78.5 ± 3.9 to 59.7 ± 1.5 Ma (N = 33: Yuguchi et al., 2011c), zircon fission-track ages from 75.6 ± 3.3 to 52.8 ± 2.6 Ma (N = 47: Yuguchi et al., 2011c; 2019), and apatite fission-track ages from 52.1 ± 2.8 to 37.1 ± 3.6 Ma (N = 33: Yamasaki and Umeda, 2012; Yuguchi et al., 2017). Such thermochronological data allowed for estimation of position-by-position cooling (time-temperature) paths within the Toki granite (Yuguchi et al., 2019). The extent of microperthite and patchperthite growth can be an indicator of the cooling process of the Toki granite (Yuguchi et al., 2011a, b). The systematic variation in development of microperthite indicates that the Toki granite cooled effectively from the paleo-roof boundary (roof boundary at the time of granitic magma intrusion) during the exsolution coarsening stage (690–780 °C) (Yuguchi et al., 2011a), while those of patchperthite indicate that the Toki granite cooled effectively from the paleo-roof boundary and from the western margin during the deuteric coarsening stage (< 500 °C) (Yuguchi et al., 2011b). The geology and petrography of the Toki granite have been described in detail by Yuguchi et al. (2010; 2011a, b, and c; 2020).

Sampling and analytical procedures

Nine samples were collected from six boreholes in all three rock facies in the Toki granite for petrographic observations and analyses of CL patterns (Fig. 1C): samples No. 1 (DH6-28), 2 (DH10-14), and 4 (DH13-8) are from the MBG lithofacies; samples No. 5 (DH13-15), 6 (MIU2-13), and 9 (MIZ1-17) are from the HBG; and samples No. 3 (DH11-31), 7 (MIU2-34), and 8 (MIZ1-06) are from the BG lithofacies (Table S1). The petrographic data used in this study were obtained from thin sections. Thin sections were prepared for electron microprobe analysis by polishing with progressively finer diamond pastes (particle sizes of 3 μm, 1 μm, and 0.25 μm) to remove any surface irregularities that can seriously affect the CL imaging quality (Frelinger et al., 2015). Thin sections with thicknesses of 30–40 μm were produced to obtain mineral chemistry using the electron probe micro-analyzer (EPMA).

CL images were generated using a scanning electron microscope (SEM) cathodoluminescence. BSE and CL images were obtained using a JEOL IT100A SEM equipped with a Gatan mini-CL detector at Yamagata University, Japan, which was operated at an accelerating voltage of 15 kV and a beam current of 1.0 nA. The SEM-CL technique is well-suited for detailed CL imaging due to its high resolution and magnification capabilities, which allow for high-quality imaging of distinct CL textures compared to optical-CL imaging (Frelinger et al., 2015). The intensity of the SEM-CL emission depends on the variations in the internal chemistry and structure of a K-feldspar crystal. The variations in the luminescence depend on the differences in minor concentrations of titanium in K-feldspar, which acts as a CL activator (Lee et al., 2007;

This is the peer-reviewed, final accepted version for American Mineralogist, published by the Mineralogical Society of America.
The published version is subject to change. Cite as Authors (Year) Title. American Mineralogist, in press.
DOI: https://doi.org/10.2138/am-2022-8146. http://www.minsocam.org/

Parsons et al., 2008; Kayama et al., 2010). Słaby et al. (2008) described that the CL intensity difference in K-feldspar is controlled by the density of Al-O$^-$-Al structural defects resulting from the coupled substitution of Ba^{2+} for K^+ and Al^{3+} for Si^{4+}. Therefore, the intensities of the SEM-CL emissions can be used to interpret the element partitioning between the melt and crystal during the mineral growth process.

Mineral element compositions and elemental maps were obtained using an EPMA (JEOL JXA-8900) with a wavelength-dispersive X-ray spectrometer (WDS) at Yamagata University. The analytical conditions for the quantitative determination of mineral compositions were as follows: an acceleration voltage of 15 kV, a beam current of 10 nA, a beam diameter of 3 μm, and the ZAF data correction method. The respective peak and background counting times were 200 s and 100 s for Ti (PET crystals) and Fe (LIF); 100 s and 50 s for Sr (TAP) and Rb (PET); 60 s and 30 s for Mn (LIF), Mg (TAP), and Ba (PET); and 10 s and 5 s for Si (TAP), Al (TAP), Ca (PET), Na (TAP), and K (PET). WDS elemental maps were obtained using the following operating conditions: 15 kV acceleration voltage, 20 nA beam current, and 200 ms dwell time per spot. Distributions of silicon, titanium, aluminum, iron, manganese, magnesium, calcium, sodium, potassium, barium, lead, and strontium were analyzed during WDS elemental mapping.

Petrography and mineralogy

Petrography of the samples

The major mineral assemblage of the MBG consists of quartz + plagioclase + K-feldspar + biotite + muscovite; that of the HBG includes quartz + plagioclase + K-feldspar + biotite + hornblende ± muscovite; and that of the BG consists of quartz + plagioclase + K-feldspar + biotite. The boundaries of the three lithofacies are defined by the appearance (MBG/HBG) and disappearance (HBG/BG) of hornblende (Yuguchi et al., 2010). All studied samples contain K-feldspar crystals. The modes of quartz, plagioclase, K-feldspar, and biotite in each thin section are 20–41, 19–36, 27–51, and 0–7 vol%, respectively, corresponding to monzogranite, granite, and granodiorite (see Fig. 7 in Yuguchi et al., 2010). Plagioclase occurs as subhedral to euhedral 1,000–20,000 μm-long crystals, quartz as anhedral to euhedral 500–25,000 μm-long crystals, and K-feldspar as anhedral 1,000–12,000 μm-long crystals. Biotite has undergone variable degrees of alteration and is partially or completely replaced by chlorite.

K-feldspar

All examined K-feldspar grains are anhedral (N = 54, Fig. 2A-1 and 2B-1), showing microperthite and patchperthite textures (Figs. 2C-1, 2D-1, 3A-1, and 3B-1). The albite-rich lamellae in microperthite are thinner and more elongate than albite-rich phases in patchperthite. The interface between the albite-rich lamellae and host phase in microperthite is sharp, whereas the interface in patchperthite is irregular. Albite-rich phases of patchperthite occur in either bead or patch form (Fig. 3A-1 and 3B-1). Hashimoto et al.

(2005) suggested that an exsolution reaction in alkali feldspar is responsible for the formation of microperthite with micrometer-scale albite-rich phases and cryptoperthite with nanometer-scale albite-rich phases. Patchperthite was formed by dissolution and reprecipitation during hydrothermal alteration (Worden et al., 1990). The formation conditions of microperthite and patchperthite correspond to the exsolution coarsening stage (690–780 °C) and deuteric dissolution–precipitation coarsening stage (<500 °C), respectively (Yuguchi et al., 2011A; 2011B). Patchperthite formed later than microperthite during sub-solidus cooling.

Results and discussion

Characterization of CL patterns of magmatic K-feldspar crystals

In this study, CL images of fifty-four K-feldspar crystals were obtained. The CL patterns of the K-feldspar crystals can be broadly divided into two categories based on the presence or absence of oscillatory zoning. Oscillatory zoning was observed in forty-two K-feldspar crystals as the cyclic alternation of dark and bright bands of luminescence (Fig. 2). Oscillatory zoning can be further categorized into two types: single crystal core oscillatory zoning (SCOZ; Fig. 2) and multiple crystal core oscillatory zoning (MCOZ; Fig. 3).

Single core oscillatory zoning. The SCOZ (Fig. 2) is defined as oscillatory zoning defining a single crystal core within K-feldspar crystals in the CL image. Thirty-seven K-feldspar crystals with major axes longer than ~1,000 μm show SCOZ patterns (Fig. 2). The SCOZ exhibits linear and curved boundaries between luminescence bands (Fig. 2). The SCOZ pattern is the most abundant in K-feldspars from the BG lithofacies: fifteen grains in the observed K-feldspars from the BG (total K-feldspars are $N = 19$), nine grains from the HBG (total $N = 16$), and nine grains from the MBG (total $N = 19$).

Based on the analysis of the CL pattern, the nucleation and crystal growth behavior of K-feldspar can be determined. The crystal cores reflect the nucleus of the K-feldspar. For example, the crystal cores of K-feldspar grains No. 3 (DH11-31)-4, 9 (MIZ1-17)-7, and 3 (DH11-31)-5 are shown in Fig. 2A-3, B-3, and C-3, respectively. The luminescence intensities of the crystal cores of the K-feldspar crystals vary. Cores with high-intensity luminescence are observed in grains No. 3 (DH11-31)-4, 9 (MIZ1-17)-7, and 3

(DH11-31)-5 (Fig. 2A-2, B-2, and C-2) and low-luminescence cores are identified in grain No. 3 (DH11-31)-7 (Fig. 2D-2). The difference in luminescence intensities of crystal cores may be due to different sectioning locations of each K-feldspar crystal during the preparation of thin sections. As oscillatory zoning consists of the multiple growth shells in three dimensions (Shore and Fowler, 1996), such sectioning effects can influence the evaluation of the oscillatory zoning within the mineral. While the geometric core of K-feldspar grain No. 9 (MIZ1-17)-7 corresponds to the crystal core (Fig. 2B), the geometric cores of grains No. 3 (DH11-31)-4, 3 (DH11-31)-5, and 3 (DH11-31)-7 do not correspond to the crystal cores (Fig. 2A, C, and D). The crystals grew within the melt until they intercepted previously crystallized minerals. For K-feldspar grain No. 3 (DH11-31)-7, the crystal grew along the X and Y directions on the observation surface of the thin section (Fig. 2D-3). The growth of the crystal along the Y-direction was stopped by a euhedral quartz, while the growth along the X-direction continued. The outer rim of the oscillatory zoning away from the crystal core is not well defined. The outside region around the K-feldspar nucleus in grain No. 3 (DH11-31)-7, e.g., α region in Fig. 2D-3, does not show any oscillatory zoning.

Multiple core oscillatory zoning. The MCOZ (Fig. 3) is defined as a pattern in which two or more crystal cores are present in the K-feldspar grains. The K-feldspar crystal of grain No. 4-1 is a coarse-grained crystal with a size of 3,210 × 2,594 μm, which shows an MCOZ pattern with five cores in the CL image (Fig. 3A-2 and A-3). All five crystal cores visible in CL show the same extinction angle under polarized light, indicating the same crystal orientation; such characteristics cannot be explained by a simple assemblage of several SCOZs. The MCOZ patterns are observed in five grains, all of which are relatively coarse-grained crystals up to ~3,000 μm in length. The crystals with MCOZs exhibit rounded boundaries between luminescence zonings (Fig. 3A-2 and B-2) and their patterns contain two to five crystal cores within a grain (Fig. 3A-3 and B-3). The crystal cores in the MCOZ exhibit low luminescence (Fig. 3A-2 and B-2). The existence of multiple crystal cores in K-feldspar grains reveals multiple nucleii.

Unzoned CL pattern. The K-feldspar grains without zoning are characterized by homogeneous luminescence across the grain (Fig. 4). These patterns do not have crystal cores, that is, they cannot be used to determine any nucleii. Among studied samples, twelve relatively small (less than ~700 μm long) grains lack any zoning. The K-feldspars with unzoned CL patterns are the most abundant in the MBG among the three lithofacies in the Toki granite: BG ($N = 2$), HBG ($N = 2$), and MBG ($N = 8$).

CL intensity and chemistry of K-feldspar.

In previous studies, variations in luminescence were explained by differences in either: 1) minor concentrations of titanium in K-feldspar (Lee et al., 2007; Parsons et al., 2008; Kayama et al., 2010), or 2) the density of Al-O^{-}-Al structural defects (Słaby et al., 2008). Figures 5 and S1 show the WDS elemental maps of SCOZ K-feldspar grains No. 3 (DH11-31)-4 and No. 9 (MIZ1-17)-7, respectively, which are illustrated by elemental distributions of silicon, titanium, aluminum, calcium, sodium, potassium, and barium.

Comparing the WDS elemental maps and CL images, there are weak correlations between titanium concentrations and CL intensity (Fig. 5A-1 and 5C). High barium concentration areas correspond to high CL intensity areas and low barium areas correspond to low CL intensity areas (Fig. 5A-1 and 5H). Figure 6 shows chemical variations in SiO_2, TiO_2, Al_2O_3, Na_2O, K_2O, and BaO along the transect line from 0 μm (the core) to 1164 μm (the rim) in the SCOZ K-feldspar grain No. 3 (DH11-31)-4. Chemical variations from cores to rims in K-feldspars display high TiO_2 concentrations (> 0.01 wt%; Fig. 6C) and high BaO concentrations (> 0.10 wt%; Fig. 6F) in high CL intensity areas, confirming a causal relationship. The positive correlation between CL intensity and titanium concentration confirms that titanium acts as a CL activator. Barium incorporation causes local structural distortions due to coupled KSi–BaAl exchange (Viswanathan and Brandt, 1980; Viswanathan and Kielhorn,1983). The KSi–BaAl exchange causes aluminum rearrangement over the tetrahedral sites in K-feldspar, and this rearrangement increases structural disorder and the density of $Al\text{-}O^{-}\text{-}Al$ structural defects (Viswanathan and Kielhorn, 1983; Słaby et al., 2008). In the K-feldspar grain No. 3 (DH11-31)-4, chemical variations in high CL intensity areas show a gradual decrease in Al_2O_3 and BaO and a gradual increase in SiO_2 and K_2O along the transect line from 167 μm to 470 μm (Fig. 6A, C, E, and F), which supports the assumption of the KSi–BaAl exchange in K-feldspar. Thus, CL variations are related to variations in the density of the $Al\text{-}O^{-}\text{-}Al$ structural defects. In summary, the CL intensity differences in K-feldspar can be attributed to the following factors: 1) variations in concentrations of titanium that acts as a CL activator, and 2) variations in the density of $Al\text{-}O^{-}\text{-}Al$ structural defects.

CL patterns of post-crystallization textures of K-feldspar.

In grain No. 8 (MIZ1-06)-2, a fine vein composed of K-feldspar and biotite cuts through a large K-feldspar grain with the SCOZ pattern (parts between arrows in Fig. 7A). The fine vein within the K-feldspar is barely identifiable in the BSE image because the vein and its host K-feldspar have almost identical chemical compositions (Fig. 7A). In contrast, in the CL image, the vein characteristics, e.g., width, direction, and length, are readily visible, with the vein displaying lower luminescence compared to the host K-feldspar grain (Fig. 7B).

The luminescence intensities of most albite-rich phases in microperthite and patchperthite are lower than those of the orthoclase-rich host phases (Fig. 8A-2, B-2, and C-2). WDS elemental maps of the SCOZ K-feldspar grain No. 2 (DH10-14)-5 (Fig. 9) and chemical compositions of albite-rich and orthoclase-rich phases in patchperthite (Table S2) indicate that the titanium and barium concentrations of the albite-rich phases are lower than those of the orthoclase-rich host phases. Figure 8A-2, B-2, and C-2 (white arrows) show that the low-luminescence albite-rich phases cut across the CL bands in the regions with oscillatory zoning. This indicates that the oscillatory zoning in the orthoclase-rich host phase was not perturbed by the formation of microperthite and patchperthite in the post-crystallization stage. In grain No. 2 (DH10-14)-5 (Fig. 8C-2), the contrast between the albite-rich phases and the orthoclase-rich host phase in patchperthite (β region) is stronger than that in microperthite (γ region). This means that the luminescence intensity of the albite-rich phase in patchperthite is lower than that in microperthite. WDS elemental maps presented in Figure 9 and chemical compositions of the albite-rich phases in microperthite and patchperthite (Table S2) show that the titanium and barium concentrations of albite-rich phases in patchperthite are lower than those in microperthite. An exception is that the albite-rich phase in patchperthite in the region without oscillatory zoning shows higher luminescence intensity than the host phase (e.g., α region of grain No. 3 (DH11-31)-7; Fig. 2D-3). WDS elemental maps of the α region in patchperthite display: 1) high calcium concentrations of the albite-rich phases relative to the orthoclase-rich host phases, and 2) homogeneous distribution of titanium, aluminium, and barium in the albite-rich and orthoclase-rich host phases (Fig. S2). Although the albite-rich phases with low luminescence are accompanied with high concentrations of calcium and aluminium (Fig. 9), the albite-rich phase with high luminescence in the α region is characterized by constant aluminium and increased calcium concentrations (Fig. S2). Thus, the high CL intensity of the albite-rich phase may be derived from Al-O^{-}-Al structural defects resulting from calcium incorporation. Mass transfer, that is, titanium and barium transfers occurred during the formation of microperthite and patchperthite. Therefore, the difference in the titanium and barium concentrations in the albite-rich phase between microperthite and patchperthite indicates the difference in their mass transfers between exsolution coarsening and deuteric dissolution–precipitation coarsening. In the exsolution coarsening stage (690–780 °C: Yuguchi et al., 2011a) when the microperthite was produced, interdiffusion between sodium and potassium essentially occurred within magmatic K-feldspar, resulting in a small amount of titanium and barium that diffused from the original distribution within the K-feldspar. Conversely, in the deuteric dissolution–precipitation coarsening stage (<

500 °C: Yuguchi et al., 2011b), titanium and barium were released from K-feldspar into the fluid, and subsequent precipitation with low titanium and barium resulted in low luminescence.

DOI: https://doi.org/10.2138/am-2022-8146. http://www.minsocam.org/

Implications

The CL analyses of perthitic anhedral K-feldspars in the equigranular Toki granite provide new insights into the nucleation and growth of magmatic K-feldspar crystals and their textural development of K-feldspar during the post-crystallization stage. Previous CL studies presented oscillatory zoning in K-feldspar megacrysts and phenocrysts in granitic rocks. It is known that K-feldspar megacrysts crystallize at super-solidus conditions in a low-temperature magma chamber or at sub-solidus conditions in granite and that K-feldspar phenocrysts crystallize in a high-temperature magma chamber. They grow in wide space between previously crystallized minerals. Anhedral K-feldspars crystallize at super-solidus conditions in a low-temperature magma chamber and grow in limited space between previously crystallized minerals. Oscillatory zoning is common in anhedral K-feldspar of equigranular granite but it may have been overlooked in previous studies. In the CL analyses, the features of nucleation and crystal growth in the limited space (anhedral K-feldspar) enable us to compare with those in the wide space (K-feldspar megacryst and phenocryst). For example, new insights from oscillatory zoning in the anhedral K-feldspar include 1) the discordance between geometric cores and crystal cores in the CL image and 2) multiple nucleii deduced from the existence of multiple crystal cores, which are uncommon in the megacryst and phenocryst studies. The detailed CL analyses, not only for anhedral K-feldspar crystals in the equigranular granite but also for K-feldspar phenocryst/megacrysts in porphyritic granite, provide insights into the nucleation and crystal growth processes of K-feldspar through the several genetic environments and thermal stages. Furthermore, the relationship between growth texture (oscillatory zoning) and chemistry reveals the spatial extent of the element partitioning between the melt and crystal and of the mass transfer from the melt into crystal during the magma evolution. The observed CL patterns can also be used to reveal the textural development in K-feldspar during the post-crystallization stage.

DOI: https://doi.org/10.2138/am-2022-8146. http://www.minsocam.org/

Acknowledgements

We acknowledge constructive reviews by Dr. D. Zhao, Dr. V. Memeti, Dr. C. Barnes (associated editor), and Dr. D.R. Baker (editor), which greatly helped with manuscript revision. We would like to thank Editage (www.editage.jp) for English language editing. This work was financially supported by the Japan Society for the Promotion of Science (JSPS) Grant for Young Scientists [grant number 16H06138], by the JSPS Grant-in-Aid for Scientific Research (B) [grant number 21H01865], and by the grant from the Ministry of Economy, Trade and Industry (METI), Japan to TY.

References

Frelinger, S.N., Ledvina, M.D., Kyle, J.R., and Zhao, D. (2015) Scanning electron microscopy cathodoluminescence of quartz: Principle, techniques and applications in ore geology. Ore Geology Reviews, 65, 840–852.

Glazner, A.F., and Johnson, B.R. (2013) Late crystallization of K-feldspar and the paradox of megacrystic granites. Contributions to Mineralogy and Petrology, 166, 777–799.

Hashimoto, K., Akai, J., and Nakano, S. (2005) Microtextures of alkali feldspar in Tanakami granite, southwest Japan and their formation process. Japanese Magazine of Mineralogical and Petrological Sciences, 34, 1–14 (in Japanese with English abstract).

Ishihara, S., and Chappell, B. (2007) Chemical compositions of the late Cretaceous Ryoke granitoids of the Chubu District, central Japan – Revisited. Bulletin of the Geological Survey of Japan, 58, 323–350.

Ishihara, S., and Suzuki, Y. (1969) Basement granites of the Toki uranium deposits in Tono region. Reports of the Geological Survey of Japan, 232, 113–127.

Itoigawa, J. (1980) Geology of the Mizunami district, central Japan. Monograph of the Mizunami Fossil Museum, 1, 1–50 (in Japanese).

Japan Nuclear Cycle Development Institute (2000) Regional Hydrogeological Study Project Result from 1992–1999. JNC Technical Report, JNC TN7400 2003-007, 86 p. Tono Geoscience Center.

Japan Nuclear Cycle Development Institute (2002) Master Plan of the Mizunami Underground Research Laboratory Project. JNC Technical Report, JNC TN7410 2003-001, 47 p. Tono Geoscience Center.

Johnson, B.R., and Glazner, A.F. (2010) Formation of K-feldspar megacrysts in granodioritic plutons by thermal cycling and late-stage textural coarsening. Contributions to Mineralogy and Petrology, 159, 599–619.

Kayama, M., Nalano, S., and Nishido, H. (2010) Characteristics of emission centers in alkali feldspar: A new approach by using cathodoluminescence spectral deconvolution. American Mineralogist, 95, 1783–1795.

Landi, P., La Felice, S., Petrelli, M., Vezzoli, L.M., and Principe, C. (2019) Deciphering textural and chemical zoning of K-feldspar megacrysts from Mt. Amiata Volcano (Southern Tuscany, Italy): Insights into the petrogenesis and abnormal crystal growth. Lithos, 324–325, 569–583.

Lee, M.R., Parsons, I., Edwards, P.R., Edwards, P.R., and Martin, R.W. (2007) Identification of cathodoluminescence activators in zoned alkali feldspars by hyperspectral imaging and electron-probe microanalysis. American Mineralogist, 92, 243–253.

Marshall, D.J. (1988) Cathodoluminescence of Geological Materials, 146 p. Hyman, Boston.

Moore, J.G., Sisson, T.W. (2008) Igneous phenocrystic origin of K-feldspar megacrysts in granitic rocks from the Sierra Nevada batholith. Geosphere, 4, 387–400.

Nakano, S., Akai, J., and Shimobayashi, N. (2005) Contrasting Fe-Ca distributions and related microtextures in syenite alkali feldspar from the Patagonia Andes, Chile. Mineralogical Magazine, 69, 521–535.

Oppenheim, L.F., Memeti, V., Barnes, C.G., Chambers, M., Krause, J., and Esposity, R.

(2021) Feldspar recycling across magma mush bodies during the voluminous Half Dome and Cathedral Peak stages of the Tuolumne intrusive complex, Yosemite National Park, California, USA. Geosphere, 17, 322–351.

Parsons, I., Steele, D.A., Lee, M.R., and Magee, C.W. (2008) Titanium as a cathodoluminescence activator in alkali feldspars. American Mineralogist, 93, 875–879.

Sano, H., Yamagata, T., and Horibo, K. (1992) Tectonostratigraphy of Mino terrane: Jurassic accretionary complex of southwest Japan. Palaeogeography, Palaeoclimatology, Palaeoecology, 96, 41–57.

Shibata, K., and Ishihara, S. (1979) Rb–Sr whole-rock and K–Ar mineral ages of granitic rocks in Japan. Geochemical Journal, 13, 113–119.

Shore, M., and Fowler, A.D. (1996) Oscillatory zoning in minerals: A common phenomenon. Canadian Mineralogist, 34, 1111–1126.

Słaby, E., Götze, J., Wörner, G., Simon, K., Wrzalik, R., and Śigielski, M. (2008) K-feldspar phenocrysts in microgranular magmatic enclaves: A cathodoluminescence and geochemical study of crystal growth as a marker of magma mingling dynamics. Lithos, 105, 85–97.

Sonehara, T., and Harayama, S. (2007) Petrology of the Nohi Rhyolite and its related granitoids: A Late Cretaceous large silicic igneous field in central Japan. Journal of Volcanology and Geothermal Research, 167, 57–80.

Suzuki, K., and Adachi, M. (1998) Denudation history of the high T/P Ryoke metamorphic belt, southwest Japan: Constraints from CHIME monazite ages of gneisses and granitoids. Journal of Metamorphic Geology, 16, 27–37.

Vernon, R.H. (1986) K-feldspar megacrysts in granites – phenocrysts, not porphyroblasts. Earth–Science Reviews, 23, 1–63.

Vernon, R.H. (2010) Granites really are magmatic: Using microstructural evidence to refuse some obstinate hypotheses. In M.A. Forster and J.D. FitzGerald, Eds., Journal of the Virtual Explorer, 35, paper 1.

Vernon, R.H., and Paterson, S.R. (2008) How late are K-feldspar megacrysts in granites? Lithos, 104, 327–336.

Viswanathan, K., and Brandt, K. (1980) The crystal structure of a ternary (Ba, K, Na)-feldspar and its significance. American Mineralogist, 65, 472–476.

Viswanathan, K., and Kielhorn, H.M. (1983) Al, Si distribution in a ternary (Ba, K, Na)-feldspar as determined by crystal structure refinement. American Mineralogist, 68, 122–124.

Worden, R.H., Walker, F.D.L., Parsons, I., and Brown, W.L. (1990) Development of microporosity, diffusion channels and deuteric coarsening in perthitic alkali feldspars. Contribution of Mineralogy and Petrology, 104, 507–515.

Yamasaki, S., and Umeda, K. (2012) Cooling history of the Cretaceous Toki granite in the eastern Sanyo Belt, Central Japan. Japanese Magazine of Mineralogical and Petrological, 41, 39–46 (in Japanese with English abstract).

Yuguchi, T., Amano, K., Tsuruta, T., Danhara, T., and Nishiyama, T. (2011c) Thermochronology and the three-dimensional cooling pattern of a granitic pluton: An example of the Toki granite, Central Japan. Contributions to Mineralogy and Petrology, 162, 1063–1077.

Yuguchi, T., Iwano, H., Kato, T., Sakata, S., Hattori, K., Hirata, T., Sueoka, S., Danhara, T., Ishibashi, M., Sasao, E., and Nishiyama, T. (2016) Zircon growth in a granitic pluton with specific mechanisms, crystallization temperatures and U–Pb ages: Implication to the 'spatiotemporal' formation process of the Toki granite, central Japan. Journal of Mineralogical and Petrological Sciences, 111, 9–34.

Yuguchi, T., Ogita, Y., Kato, T., Yokota, R., and Nishiyama, T. (2020) Crystallization processes of quartz in a granitic magma: Cathodoluminescence zonation pattern controlled by temperature and titanium diffusivity. Journal of Asian Earth Sciences, 192, 104289.

Yuguchi, T., Sueoka, S., Iwano, H., Danhara, T., Ishibashi, M., Sasao, E., and Nishiyama, T. (2017) Spatial distribution of the apatite fission-track ages in the Toki granite, central Japan: Exhumation rate of a Cretaceous pluton emplaced in the East Asian continental margin. Island Arc 26, e12219.

Yuguchi, T., Sueoka, S., Iwano, H., Izumino, Y., Ishibashi, M., Danhara, T., Sasao, E., Hirata, T., and Nishiyama, T. (2019) Position-by-position cooling paths within the Toki granite, central Japan: Constraints and the relation with fracture population in a pluton. Journal of Asian Earth Science, 169, 47–66.

Yuguchi, T., Tsuruta, T., and Nishiyama, T. (2010) Zoning of rock facies and chemical composition in the Toki granitic body, Central Japan. Japanese Magazine of Mineralogical and Petrological Sciences, 39, 50–70 (in Japanese with English abstract).

Yuguchi, T., Tsuruta, T., and Nishiyama, T. (2011a) Three-dimensional cooling pattern of a granitic pluton I: The study of exsolution sub-solidus reactions in the Toki granite, Central Japan. Journal of Mineralogical and Petrological Sciences, 106, 61–78.

Yuguchi, T., Tsuruta, T., and Nishiyama, T. (2011b) Three-dimensional cooling pattern of a granitic pluton II: The study of deuteric sub-solidus reactions in the Toki granite, Central Japan. Journal of Mineralogical and Petrological Sciences, 106, 130–141.

Figure captions

Figure 1. The Toki granite. (A) Map of Southwest Japan showing the location of the Toki granite (square symbol) in central Japan and the distribution of the San-in, Sanyo, and Ryoke belts in the inner zone of Southwest Japan (modified after Ishihara and Chappell, 2007). (B) Geologic map of the Toki granite showing the borehole sites (modified after Itoigawa, 1980). The topographic contours in the Tono district are based on topographic maps of the Geographical Survey Institute (1:25,000) titled "Mitake," "Takenami," "Toki," and "Mizunami". Borehole investigations of the Toki granite were performed by the Japan Atomic Energy Agency (Japan Nuclear Cycle Development Institute 2000, 2002). (C) Rock facies cross-section of the Toki granite along the X to X' transect of the geologic map (Fig. 1B). MBG: muscovite–biotite granite, HBG: hornblende–biotite granite, and BG: biotite granite (Yuguchi et al. 2010).

Figure 2. Backscattered electron (BSE: A-1, B-1, C-1, and D-1) and cathodoluminescence (CL: A-2, B-2, C-2, and D-2) images of K-feldspar crystals showing SCOZ patterns (A: grain No. 3 (DH11-31)-4, B: grain No. 9 (MIZ1-17)-7, C: grain No. 3 (DH11-31)-5, and D: grain No. 3 (DH11-31)-7). The CL images reveal the crystal core parts displayed in CL images (crystal core: A-3, B-3, and C-3) and crystal growth direction (D-3). If the nucleus of K-feldspar crystallization in grain No. 3 (DH11-31)-7 is defined as the origin of growth, "0 μm", the regions beyond 480 μm in the X-direction and 270 μm in the Y-direction do not show oscillatory zoning (α region) (2D-3).

Figure 3. Backscattered electron (BSE: A-1 and B-1) and cathodoluminescence (CL: A-2 and B-2) images of K-feldspar crystals showing MCOZ patterns (A: grain No. 4 (DH13-8)-1, and B: grain No. 4 (DH13-8)-3). The CL images reveal the nucleii displayed in CL images (crystal core: A-3 and B-3).

Figure 4. Backscattered electron (BSE: A-1 and B-1) and cathodoluminescence (CL: A-2 and B-2) images of K-feldspar crystals showing unzoned CL patterns (A: grain No. 1 (DH6-28)-1, and B: grain No. 1 (DH6-28)-7).

Figure 5. Backscattered electron image (A-1), cathodoluminescence image (A-2) and WDS elemental maps showing silicon (B), titanium (C), aluminum (D), calcium (E), sodium (F), potassium (G), and barium (H) of a SCOZ K-feldspar grain No. 3 (DH11-31)-4. WDS elemental maps were obtained with 3 μm step size at a resolution of up to 300 × 300 pixels.

Figure 6. WDS linescans of SiO_2 (A), TiO_2 (B), Al_2O_3 (C), Na_2O (D), K_2O (E), and BaO (F) along the scanning lines in BSE and CL images. Scanning line from 0 μm to 1164 μm in the SCOZ K-feldspar grain No. 3 (DH11-31)-4.

Figure 7. Backscattered electron (A) and cathodoluminescence (B) images of K-feldspar crystals (grain No. 8 (MIZ1-06)-2) with veins in the SCOZ (between arrows).

Figure 8. Backscattered electron (BSE: A-1, B-1, and C-1) and cathodoluminescence (CL: A-2, B-2, and C-2) images of K-feldspar crystals showing the distribution of albite-rich lamellae in microperthite and patchperthite (A: grain No. 6 (MIU2-13)-3, B: grain No. 5 (DH13-15)-8, and C: grain No. 2 (DH10-14)-5).

Figure 9. Backscattered electron image (A-1), cathodoluminescence image (A-2), and WDS elemental maps showing silicon (B), titanium (C), aluminum (D), calcium (E), sodium (F), potassium (G), and barium (H) of a SCOZ K-feldspar grain No. 2 (DH10-14)-5. WDS elemental maps were obtained with 4 μm step size and a resolution up to 260 × 260 pixels.

Figure S1. Backscattered electron image (A-1), cathodoluminescence image (A-2), and WDS elemental maps showing silicon (B), titanium (C), aluminum (D), calcium (E), sodium (F), potassium (G), and barium (H) of a SCOZ K-feldspar grain No. 9 (MIZ1-17)-7. WDS elemental maps were obtained with a 5 μm step size and a resolution up to 200 × 200 pixels.

Figure S2. Backscattered electron image (A-1), cathodoluminescence image (A-2), and WDS elemental maps showing silicon (B), titanium (C), aluminum (D), calcium (E), sodium (F), potassium (G), and barium (H) of a SCOZ K-feldspar grain No. 3(DH11-31)-7. WDS elemental maps were obtained with a 3 μm step size and a resolution up to 150 × 150 pixels.

DOI: https://doi.org/10.2138/am-2022-8146. http://www.minsocam.org/

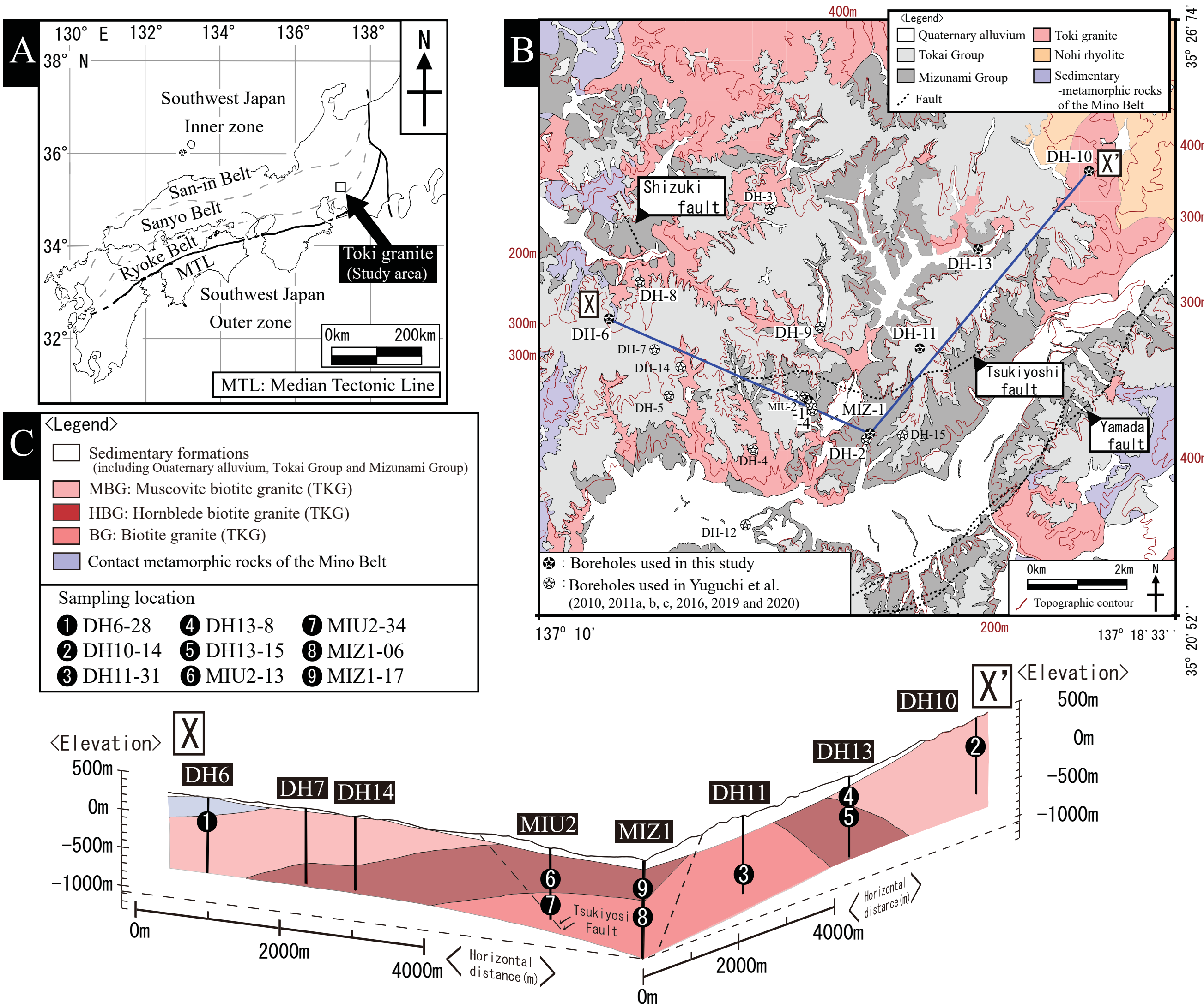

Yuguchi et al. Fig. 1

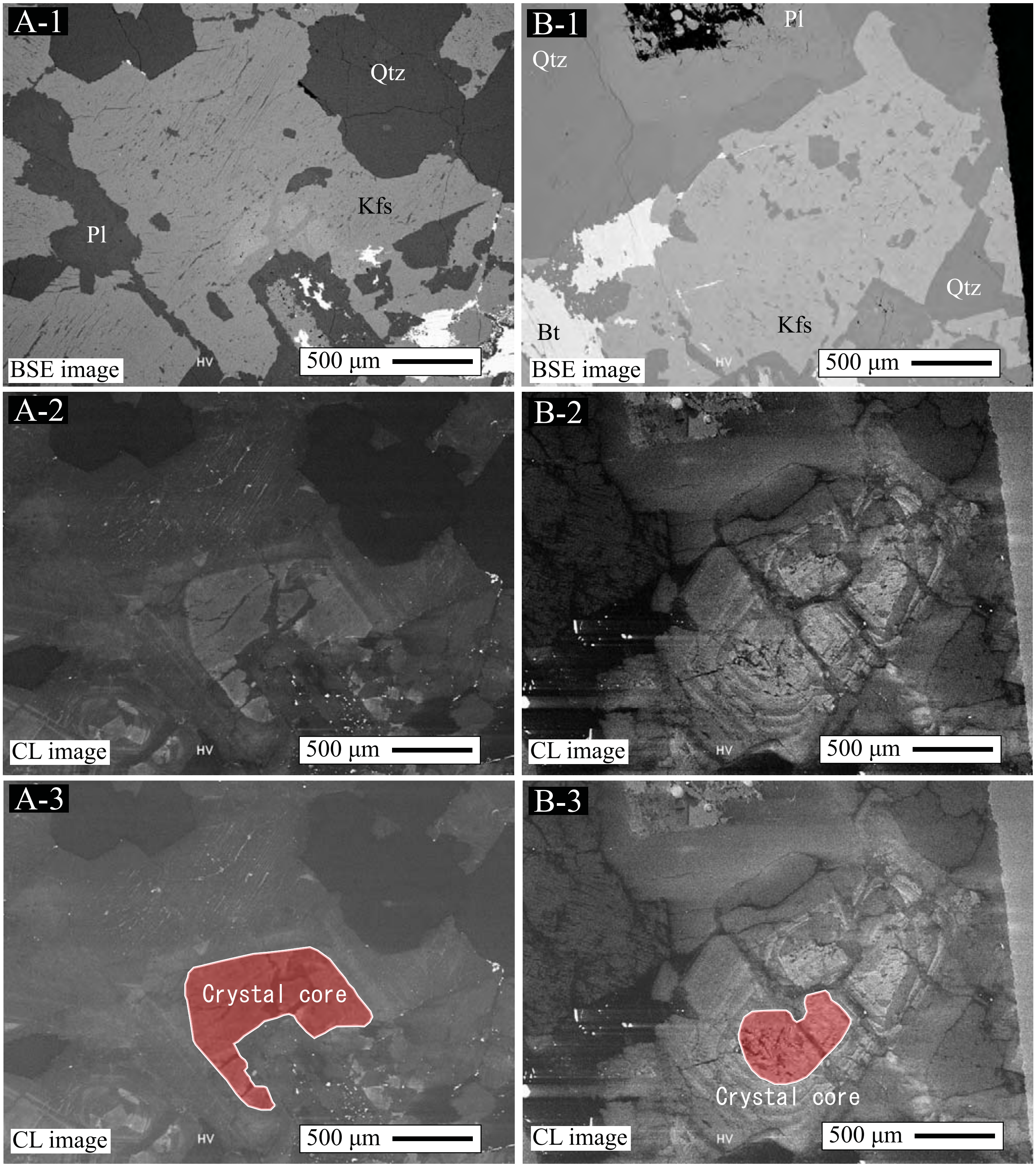

Yuguchi et al. Fig. 2

This is the peer-reviewed, final accepted version for American Mineralogist, published by the Mineralogical Society of America.
The published version is subject to change. Cite as Authors (Year) Title. American Mineralogist, in press.
DOI: https://doi.org/10.2138/am-2022-8146. http://www.minsocam.org/

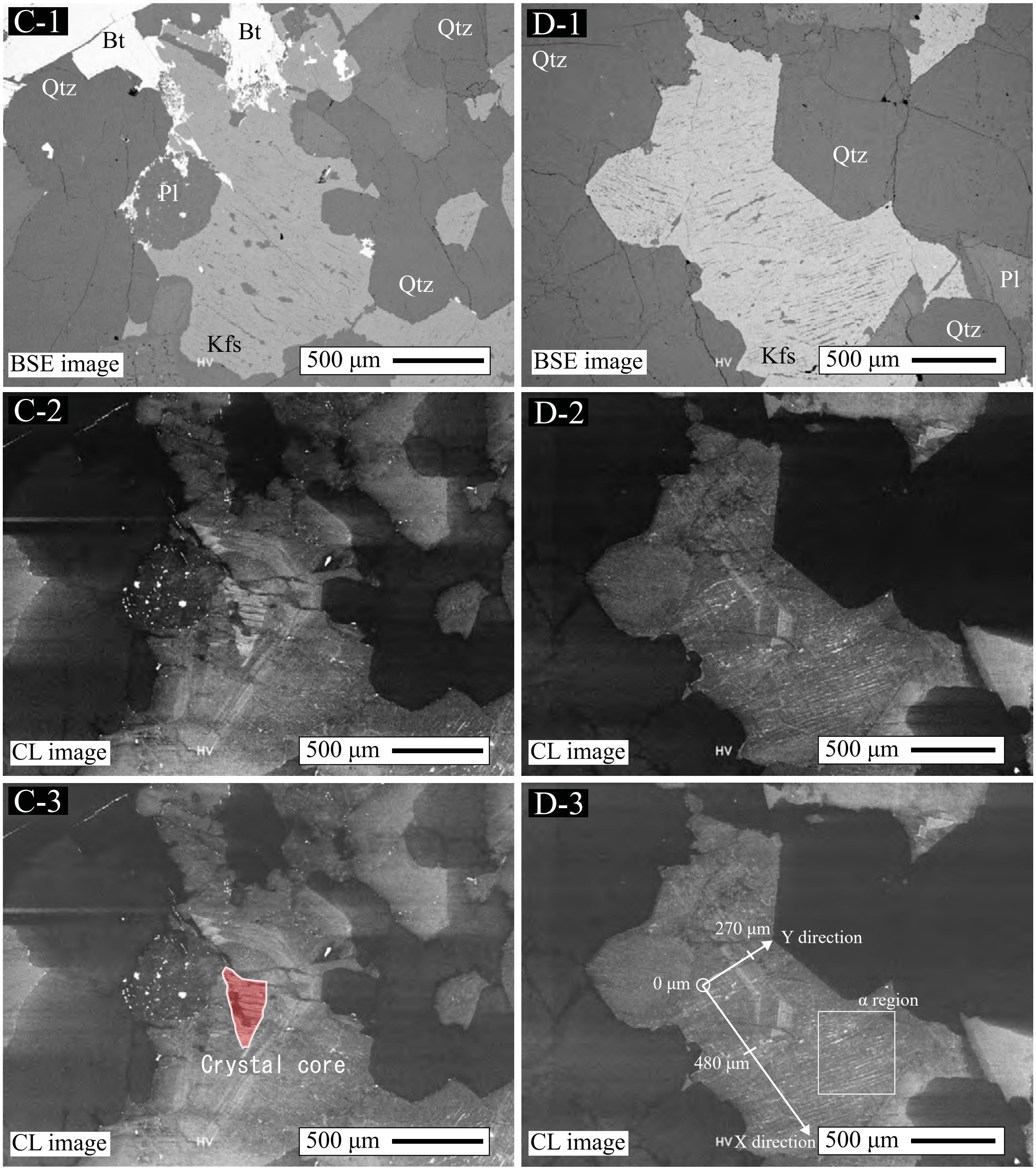

Yuguchi et al. Fig. 2 continued

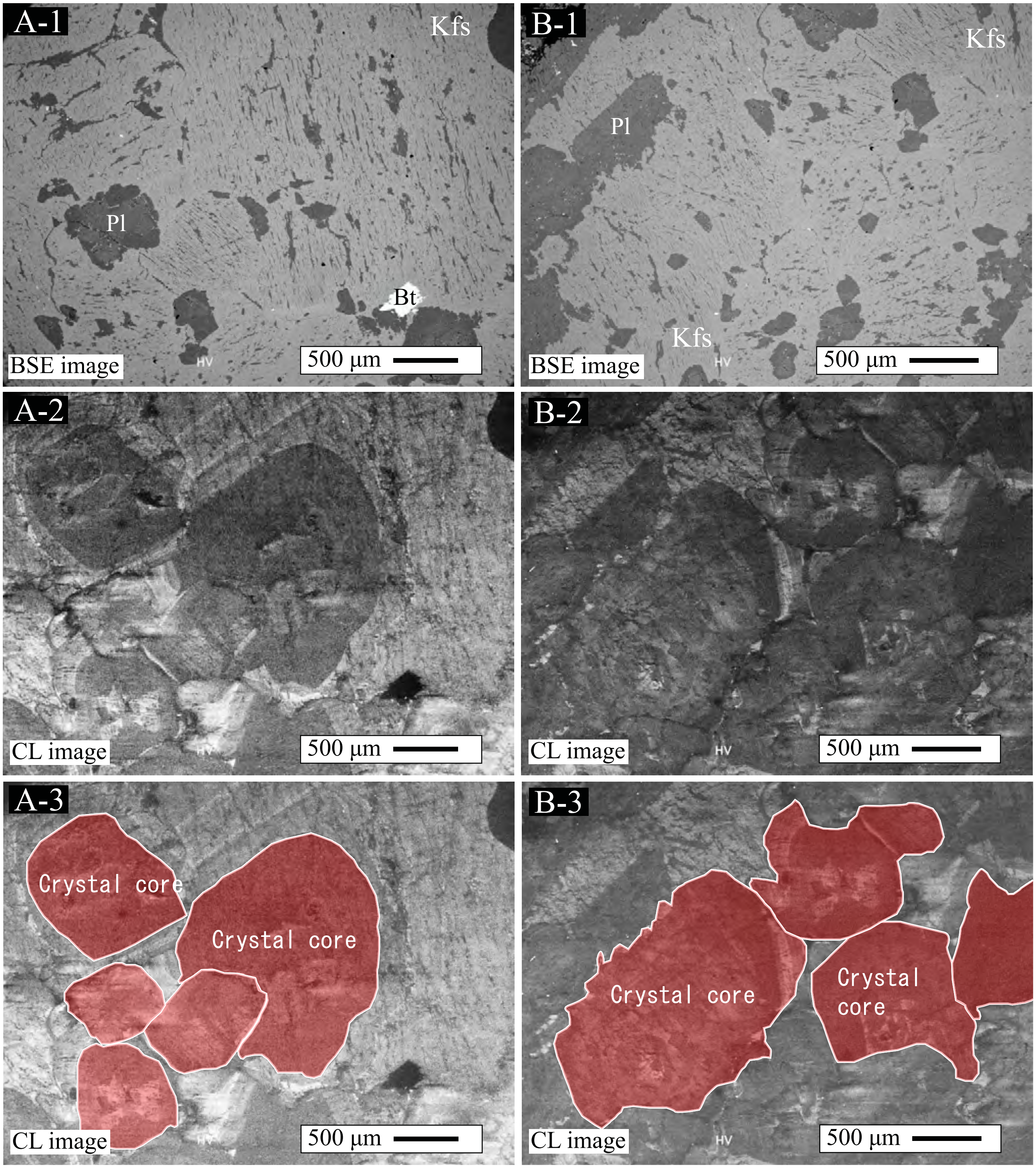

Yuguchi et al. Fig. 3

DOI: https://doi.org/10.2138/am-2022-8146. http://www.minsocam.org/

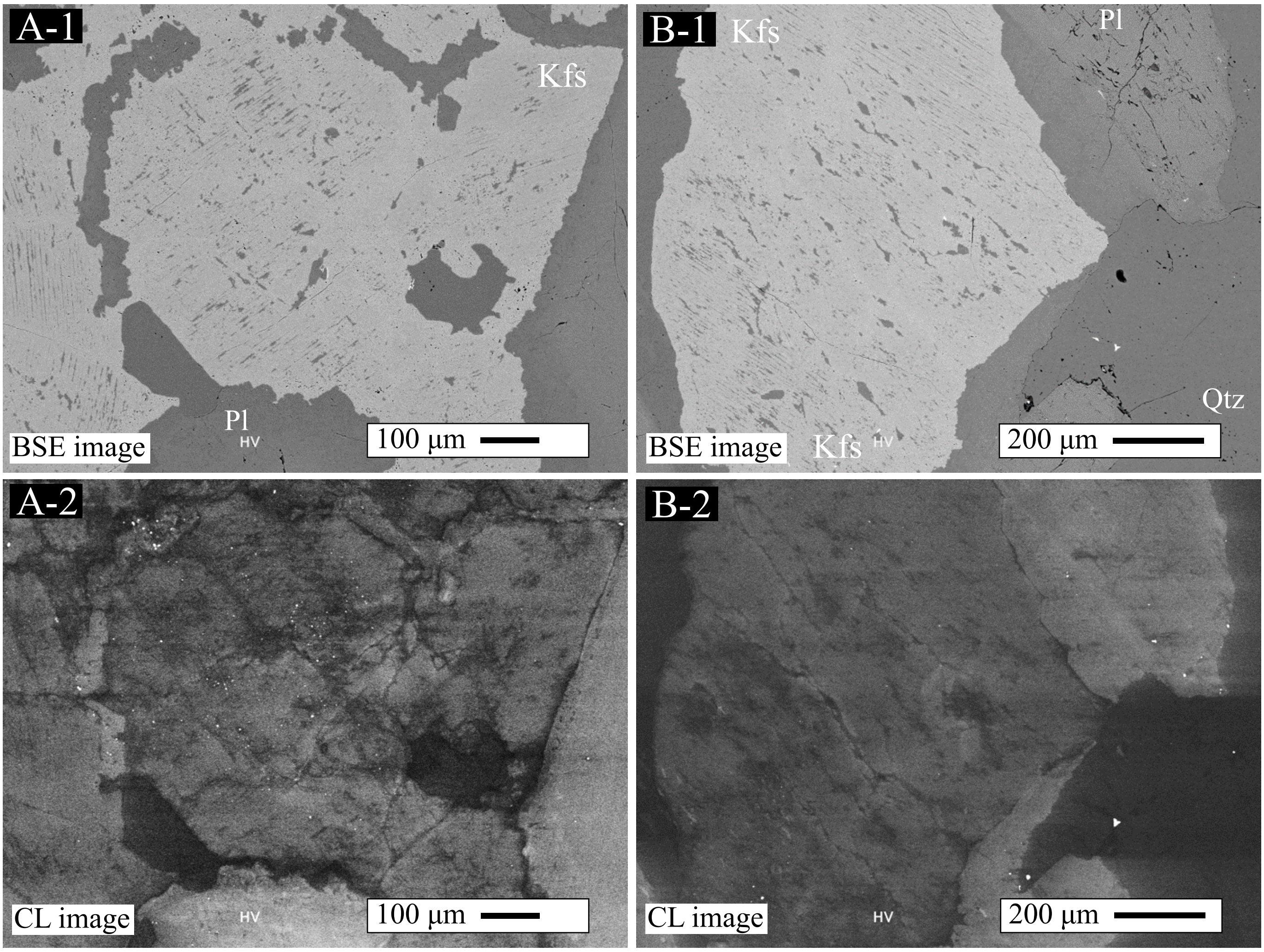

Yuguchi et al. Fig. 4

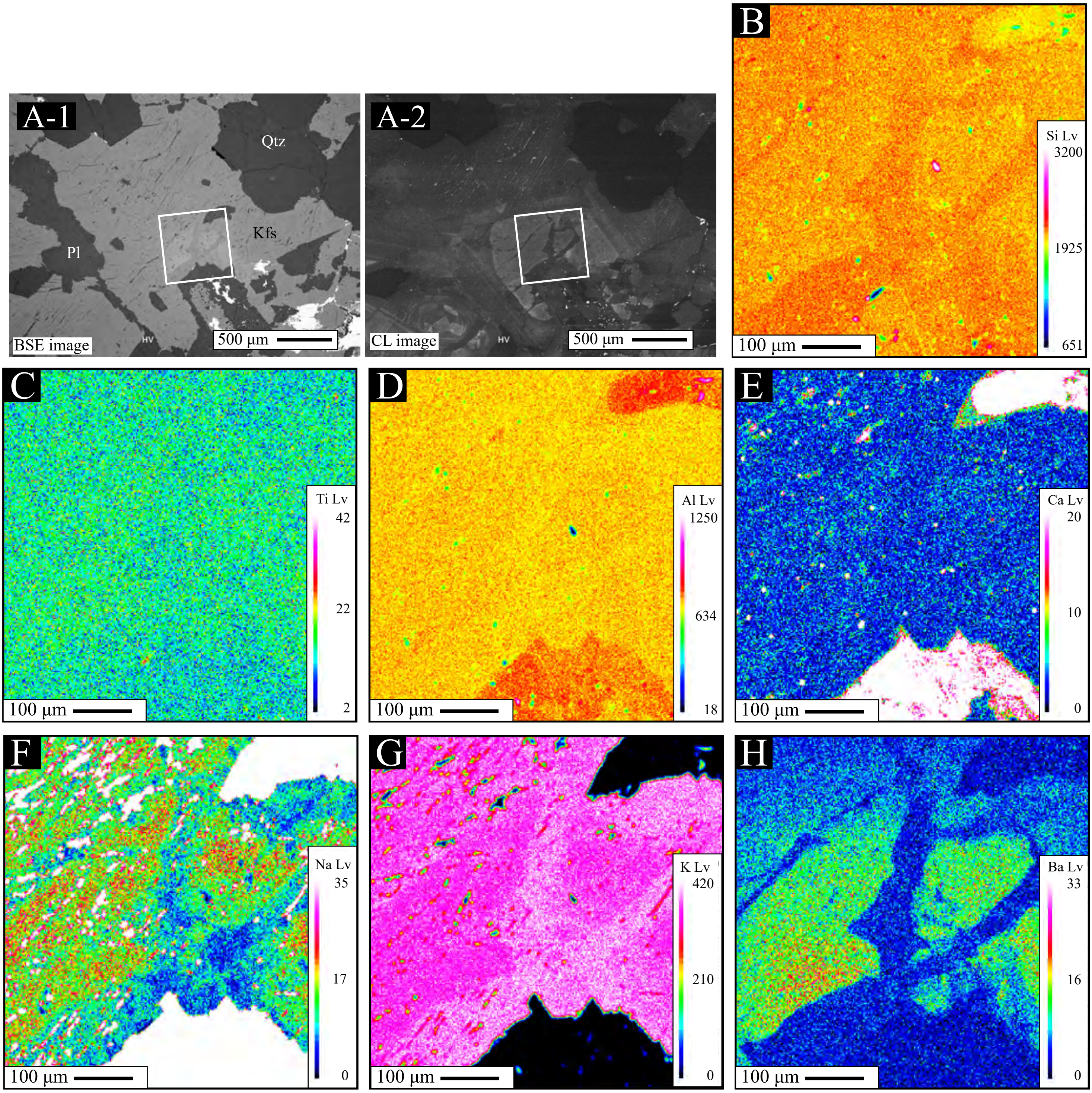

Yuguchi et al. Fig. 5

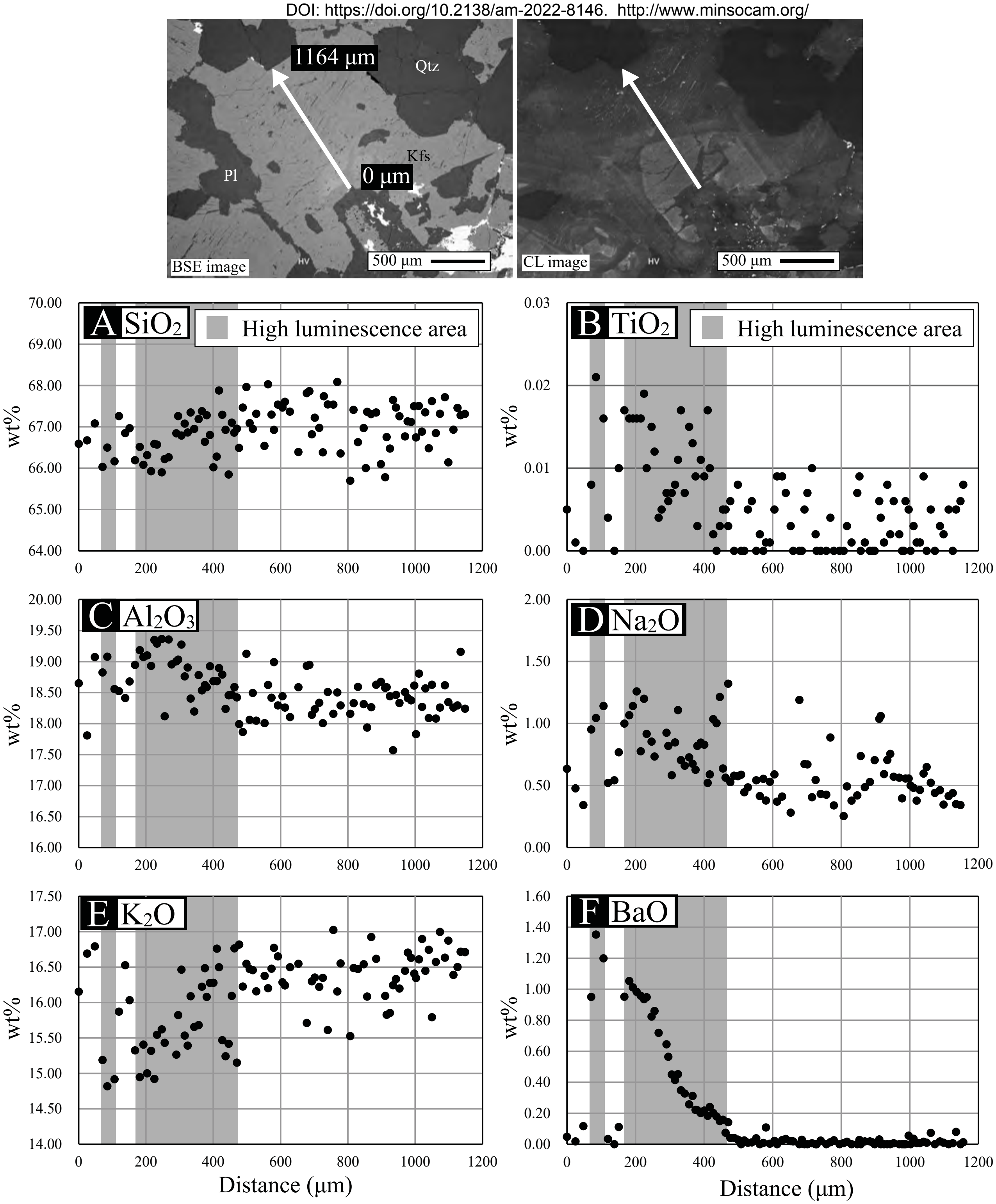

Yuguchi et al. Fig. 6

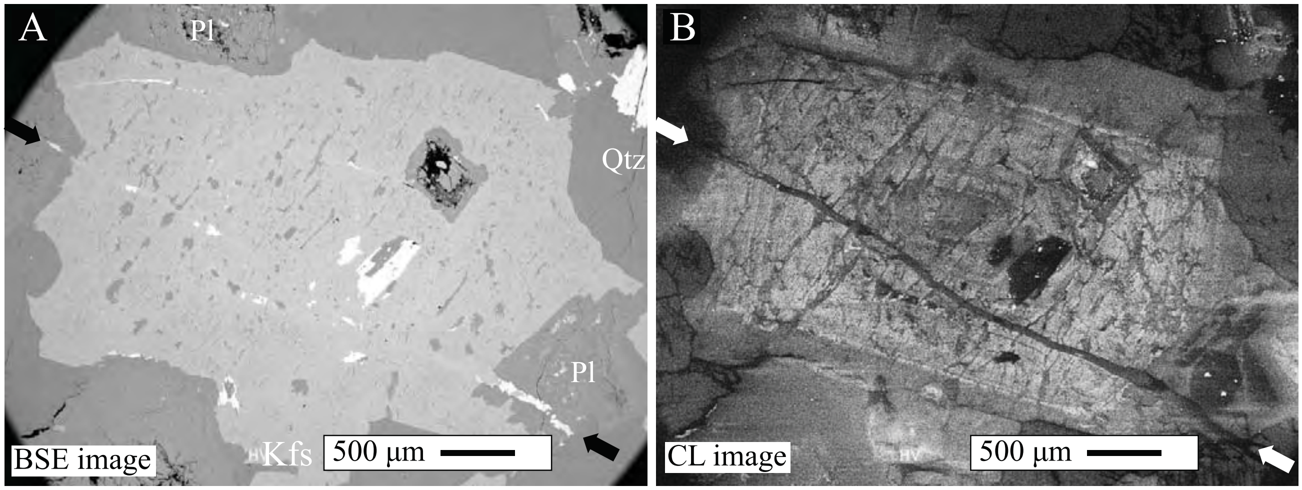

Yuguchi et al. Fig. 7

DOI: https://doi.org/10.2138/am-2022-8146. http://www.minsocam.org/

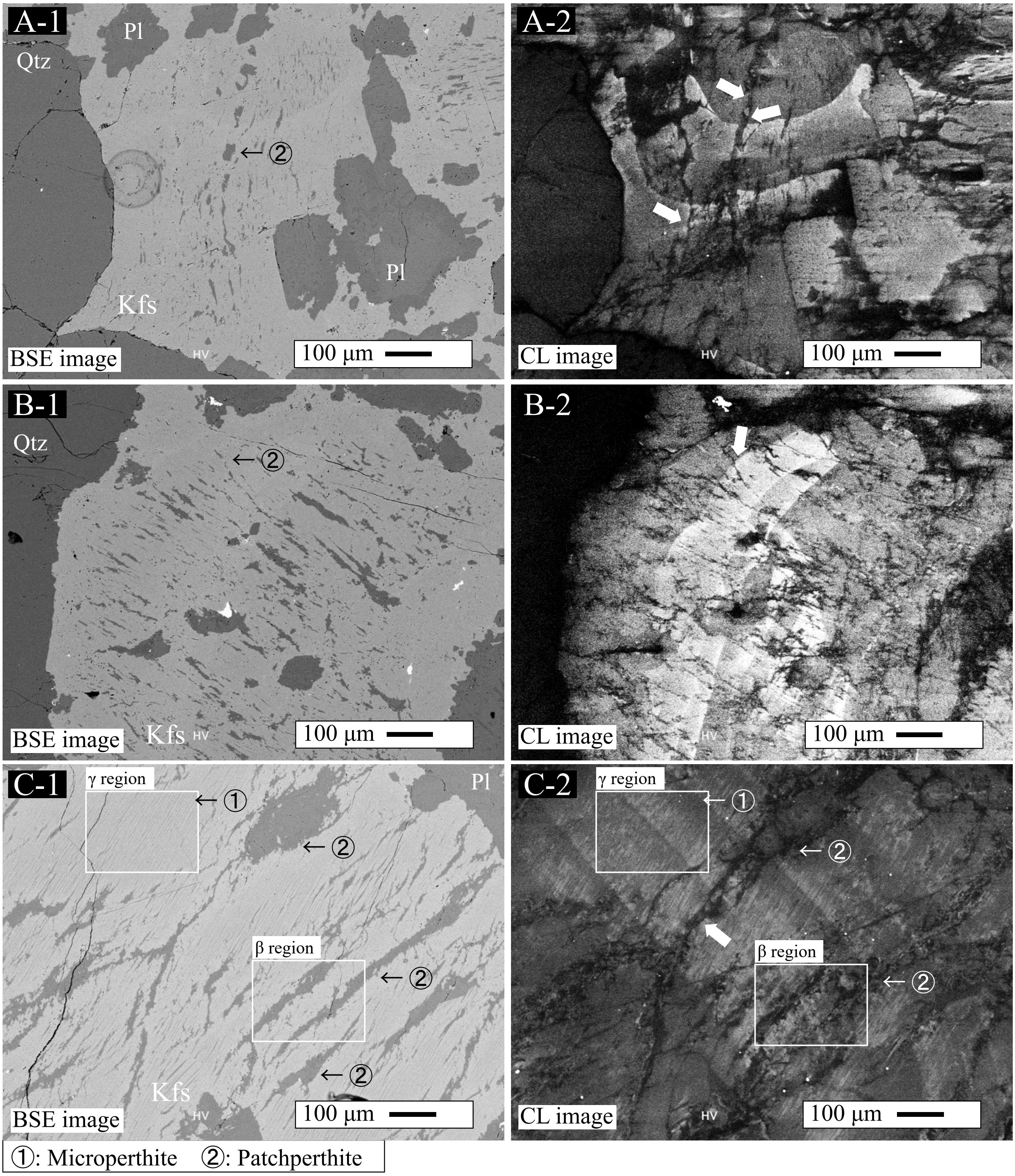

Yuguchi et al. Fig. 8

DOI: https://doi.org/10.2138/am-2022-8146. http://www.minsocam.org/

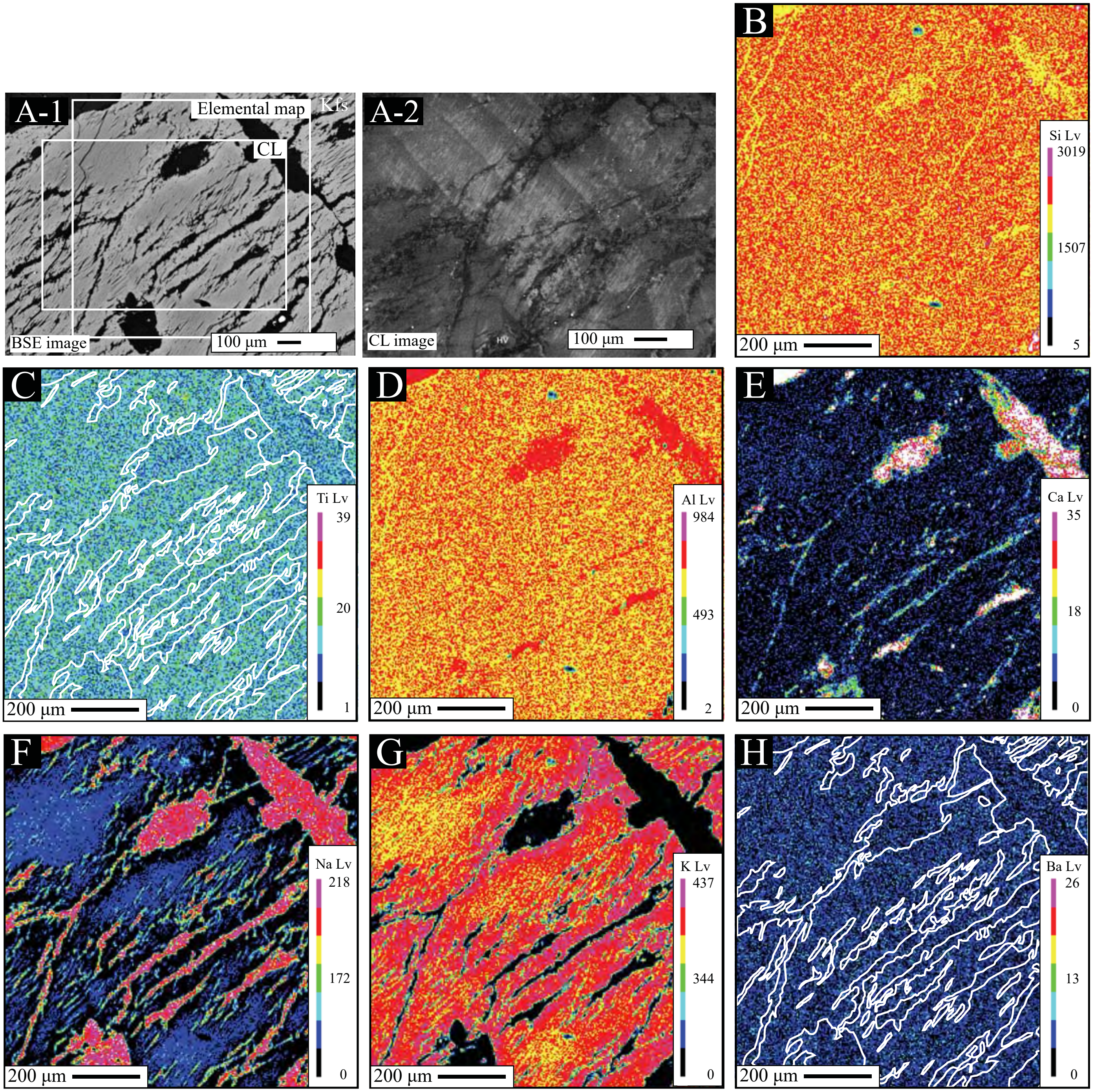

Yuguchi et al. Fig. 9